

1 Direct evidence of induced magnetic moment in Se and the role of misplaced Mn in MnBi₂Se₄-based 2 intrinsic magnetic topological insulator heterostructures

3 R. Fukushima,¹ V. N. Antonov,² M. M. Otrokov,³ T. T. Sasaki,⁴ R. Akiyama,¹ K. Sumida,^{5,*} K. Ishihara,¹ S. Ichinokura,¹ K.
4 Tanaka,⁶ Y. Takeda,^{5,†} D. P. Salinas,⁷ S. V. Eremeev,⁸ E. V. Chulkov,^{9,10,11,12,13} A. Ernst,^{14,2} and T. Hirahara^{1,‡}

5 ¹*Department of Physics, Tokyo Institute of Technology, Tokyo 152-8551, Japan*

6 ²*Institute for Theoretical Physics, Johannes Kepler University, A-4040 Linz, Austria*

7 ³*Instituto de Nanociencia y Materiales de Aragón (INMA),*

8 *CSIC-Universidad de Zaragoza, Zaragoza 50009, Spain*

9 ⁴*Research Center for Magnetic and Spintronic Materials,*

10 *National Institute for Materials Science, Tsukuba 305-0047, Japan*

11 ⁵*Materials Sciences Research Center, Japan Atomic Energy Agency, Sayo, Hyogo 679-5148, Japan*

12 ⁶*UVSOR III Synchrotron, Institute for Molecular Science, Okazaki 444-8585, Japan*

13 ⁷*ALBA Synchrotron Light Source, E-08290 Cerdanyola del Valles, Spain*

14 ⁸*Institute of Strength Physics and Materials Science, Tomsk, 634055, Russia*

15 ⁹*Donostia International Physics Center (DIPC), Paseo de Manuel Lardizabal,*

16 *4, 20018 San Sebastián/Donostia, Basque Country, Spain*

17 ¹⁰*Departamento de Física de Materiales, Facultad de Ciencias Químicas,*

18 *UPV/EHU, Apdo. 1072, 20080 San Sebastián, Basque Country, Spain*

19 ¹¹*Centro de Física de Materiales, CFM-MPC, Centro Mixto CSIC-UPV/EHU,*

20 *Apdo.1072, 20080 San Sebastián/Donostia, Basque Country, Spain*

21 ¹²*Tomsk State University, Tomsk, 634050, Russia*

22 ¹³*Saint Petersburg State University, Saint Petersburg, 198504, Russia*

23 ¹⁴*Max Planck Institute of Microstructure Physics, D-06120 Halle (Saale), Germany*

24 (Dated: August 2, 2024)

Intrinsic magnetic topological insulators, in which magnetism and topology are inherently combined, are excellent systems to realize exotic phenomena such as the quantum anomalous Hall effect. However there are many reports that show that the experimental samples are not so ideal and the effect of the unintentional disorder in these systems needs to be considered carefully. In this study, we investigate the role of misplaced magnetic atoms as well as nonmagnetic elements in the intrinsic magnetic topological insulator heterostructures based on MnBi₂Se₄ and Bi₂Se₃. We find that Mn atoms are not only placed at the central layer of the MnBi₂Se₄ septuple layer (SL) but also intermix with Bi (antisite Mn) as well as reside in the van der Waals (vdW) gap. Through a detailed comparison between the experimental and theoretical X-ray magnetic circular dichroism (XMCD) spectra, we find that the antisite Mn is coupled ferromagnetically whereas the vdW Mn couple antiferromagnetically to the Mn in the central atomic plane of the SL. Furthermore, we detect a clear XMCD signal in nonmagnetic Se, providing unambiguous evidence of its magnetic interaction with Mn.

25 I. INTRODUCTION

26 The interplay of magnetism and topological properties [1]
27 leads to exotic quantum phenomena like the quantized anoma-
28 lous Hall effect (QAHE) [2, 3], topological magnetoelectric
29 effect [4], or the half-integer quantum Hall effect [5]. Intrinsic
30 magnetic topological insulators (TIs) such as MnBi₂Te₄
31 (MBT) are materials which intrinsically possess both mag-
32 netic and topologically nontrivial properties. They are exper-
33 imentally realized both in thin films [6, 7] or in the bulk form
34 [8]. Even superlattices composed of magnetic TIs and non-
35 magnetic TIs have been fabricated [9].

36 The influence of the native defects, which are misplaced
37 Mn atoms, on the magnetic and electronic structure of the
38 compounds of the MBT family is being actively studied cur-

39 rently. Both macroscopic [10–12] and local [13] measure-
40 ments reveal that in MBT and MnSb₂Te₄ the Mn atoms in
41 the central layer of the septuple layer (SL) and those in the
42 Bi/Sb layers couple antiferromagnetically (AFM). Accord-
43 ing to the recent density functional theory (DFT) calcula-
44 tions [14], this magnetic structure may be responsible for
45 the unexpected reduction of the gap in the surface Dirac
46 cone (DC) of MBT, observed by angle-resolved photoe-
47 mission spectroscopy (ARPES) [8, 15–25]. The gap size
48 fluctuations across the surface have been visualized using
49 scanning tunneling spectroscopy (STS) for the surfaces of
50 the MnBi_{2-x}Sb_xTe₄ bulk single crystals [26] as well as the
51 molecular-beam epitaxy grown MBT [27, 28] and MnSb₂Te₄
52 [29, 30] films. As far as the cousin compound MnBi₂Se₄
53 (MBS) and heterostructures on its basis are concerned [6, 31,
54 32], the coupling of the Mn antisites to the main Mn sites
55 has not been studied yet. Especially, an element-specific as
56 well as a site-specific study that can directly correlate the lo-
57 cal magnetic properties of atoms residing at different places of
58 the sample in real space is not thoroughly conducted. Besides,
59 for intrinsic magnetic TI family, so far there has been no evi-
60 dence of induced magnetic moment in nonmagnetic elements,

* Present address: Research Institute for Synchrotron Radiation Science,
Hiroshima University, 2-313 Kagamiyama, Higashi-Hiroshima 739-0046,
Japan

† Deceased

‡ hirahara@phys.titech.ac.jp

61 although many X-ray magnetic circular dichroism (XMCD) 116
62 measurements have been performed [8, 32–39]. This is in 117
63 contrast to the case of magnetic impurity-doped TIs [40–42].

64 Therefore in the present work, we study MBS and char- 118
65 acterize the Mn distribution of MBS / Bi_2Se_3 (BS, nonmag- 119
66 netic) and MBS / n quintuple layer (QL) BS / MBSBS het- 120
67 erostructures with scanning transmission electron microscopy 121
68 (STEM) at the atomic scale. Then, this information is cor- 122
69 related with the site-specific magnetic property of the sys- 123
70 tem, focusing on the misplaced Mn and Se atoms obtained 124
71 with element-specific XMCD measurements. We find that Mn 125
72 atoms are not only placed at the central layer of the MBS SL 126
73 but also intermix with Bi as well as reside in the van der Waals 127
74 (vdW) gap. By comparing the experimental and theoretical 128
75 XMCD spectra, it is revealed that the former two couple fer- 129
76 romagnetically (FM) whereas the vdW Mn couple AFM to 130
77 the Mn in the central atomic plane of the SL. This behavior 131
78 is different from the case of MBT and is also reproduced by 132
79 directly calculating the exchange coupling constant. Further- 133
80 more, we succeed in detecting a clear XMCD signal in one 134
81 of the nonmagnetic constituents of the heterostructures - Se, 135
82 providing unambiguous evidence of its magnetic interaction 136
83 with Mn. 137

84 II. METHODS

85 The heterostructure samples were prepared by molecular 138
86 beam epitaxy in ultrahigh vacuum (UHV) chambers equipped 139
87 with a reflection-high-energy electron diffraction (RHEED) 140
88 system. First, a clean Si(111)- 7×7 surface was prepared on 141
89 an n -type substrate by a cycle of resistive heat treatments. The 142
90 7×7 surface was terminated with Bi which lead to the forma- 143
91 tion of the Si(111)- $\sqrt{3} \times \sqrt{3}$ surface. Then Bi was deposited 144
92 on the $\sqrt{3} \times \sqrt{3}$ surface at $\sim 200^\circ\text{C}$ in a Se-rich condition. 145
93 Such a procedure is reported to result in a smooth epitaxial 146
94 film formation with the stoichiometric ratio of Bi : Se = 2 : 3. 147
95 The grown Bi_2Se_3 films were annealed at $\sim 250^\circ\text{C}$ for 5 min- 148
96 utes. The thickness of the Bi_2Se_3 films in this work is ~ 8 QL. 149
97 Finally, Mn was deposited on Bi_2Se_3 in a Se-rich condition 150
98 at $\sim 250^\circ\text{C}$. In this process, Mn and Se intercalate into the 151
99 topmost QL of BS to form the MBSBS heterostructure. The 152
100 1×1 periodicity with the same lattice constant is maintained 153
101 during this process for the samples we have fabricated. Then 154
102 an additional $(n + 1)$ QL of Bi_2Se_3 was deposited on top of 155
103 the MBSBS, and then Mn and Se were intercalated to form 156
104 the MBS / n QL BS / MBSBS heterostructures (Fig. S1 (a)). 157

105 For the X-ray magnetic circular dichroism (XMCD) and 161
106 scanning transmission emission microscopy (STEM) mea- 162
107 surements, the fabricated samples were first characterized 163
108 with angle resolved photoemission spectroscopy (ARPES) at 164
109 room temperature. Then they were capped with 10 nm of Se 165
110 before taking them out of the UHV chamber. 166

111 For the XMCD measurements, the samples were annealed 167
112 at $\sim 250^\circ\text{C}$ to remove the capping layers prior to the measure- 168
113 ments. The X-ray absorption spectroscopy (XAS) and XMCD 169
114 measurements were performed at BL23SU of SPring-8 [43] 170
115 and at BL29 BOREAS of ALBA with the total-electron-yield

method [44].

117 Electron transparent specimens for STEM observations 118
119 were prepared by the standard lift-out technique using an 120
121 FEI Helios G4-UX dual-beam system. Probe aberration cor- 122
123 rected STEM, FEI TitanG2 80–200 microscope, was used. 124
125 Chemical compositions were measured by energy-dispersive 126
127 X-ray spectroscopy (EDS). EDS data was obtained for a 128
129 $2.4 \times 7.3 \text{ nm}^2$ region with a beam size of $100 \times 300 \text{ pm}^2$ that 130
131 can resolve the layered structure of Mn, Bi and Te at $\sim 0.2 \text{ nm}$ 132
133 spacing. 134

135 Electronic structure calculations were carried out within 136
137 the density functional theory (DFT) using the projector 138
139 augmented-wave (PAW) method [45] as implemented in the 140
141 VASP code [46, 47]. The Hamiltonian contained scalar rela- 142
143 tivistic corrections and the spin-orbit coupling was taken into 143
144 account by the second variation method [48]. The generalized 144
145 gradient approximation (GGA-PBE [49]) for the exchange- 145
146 correlation energy and the DFT-D3 van der Waals (vdW) func- 146
147 tional with Becke-Johnson damping [50] were applied. The 147
148 k -point mesh of $10 \times 10 \times 1$ were used to sample the slab Brill- 148
149 ouin zone. The Mn $3d$ -states were treated employing the 149
150 GGA+ U approach [51] within the Dudarev scheme [52]. The 150
151 $U_{\text{eff}} = U - J$ value for the Mn $3d$ -states was chosen to be equal 151
152 to 5.34 eV. 152

153 Exchange interactions were studied applying the magnetic 153
154 force theorem as it is implemented within the multiple scat- 154
155 tering theory [53, 54]. For that, the electronic structures of 155
156 MBT and MBS/BS were calculated using a self-consistent 156
157 Green’s function method within the density functional the- 157
158 ory [54, 55] within PBEsol approximation to the exchange- 158
159 correlation functional [56]. At that, the Mn $3d$ -states were 159
160 treated employing the GGA+ U approach [51], the U value 160
161 being equal to 3.5 eV for both MBT and MBSBS. Chemical 161
162 disorder was modeled by mixing two atomic species on the 162
163 same atomic site within the coherent potential approximation 163
164 (CPA) [57, 58]. 164

165 Theoretical XAS and XMCD simulations have been per- 165
166 formed using a linear response approach as it is implemented 166
167 within an LMTO method [59]. 167

168 To simulate the XAS and XMCD spectra as well as to cal- 168
169 culate the exchange coupling parameters the position of the 169
170 Mn atom in the vdW gap has been determined by means of 170
the total-energy calculations done using VASP. We have found 171
that the Mn atom prefers the tetrahedral vdW site (Fig. 1(f)), 172
being located practically within the vdW Se layer of the SL. 173

174 III. RESULTS AND DISCUSSIONS

175 First we discuss the atomic structure of the samples we have 175
176 fabricated. Figure 1(a) shows the STEM image of the het- 176
177 erostructure with $n = 1$ and this clearly indicates that the de- 177
178 signed structure is formed in this region. However in Fig. 1(b), 178
179 which is the STEM image of the $n = 3$ designed sample, one 179
180 can find structures of $n = 1, 3$, and 4, showing that these sam- 180
181 ples can be inhomogeneous with regions of different n coex- 181
182 isting. Furthermore, areas where the MBS layers are absent as 182
183 well as regions with three SLs were also observed. A variety 183

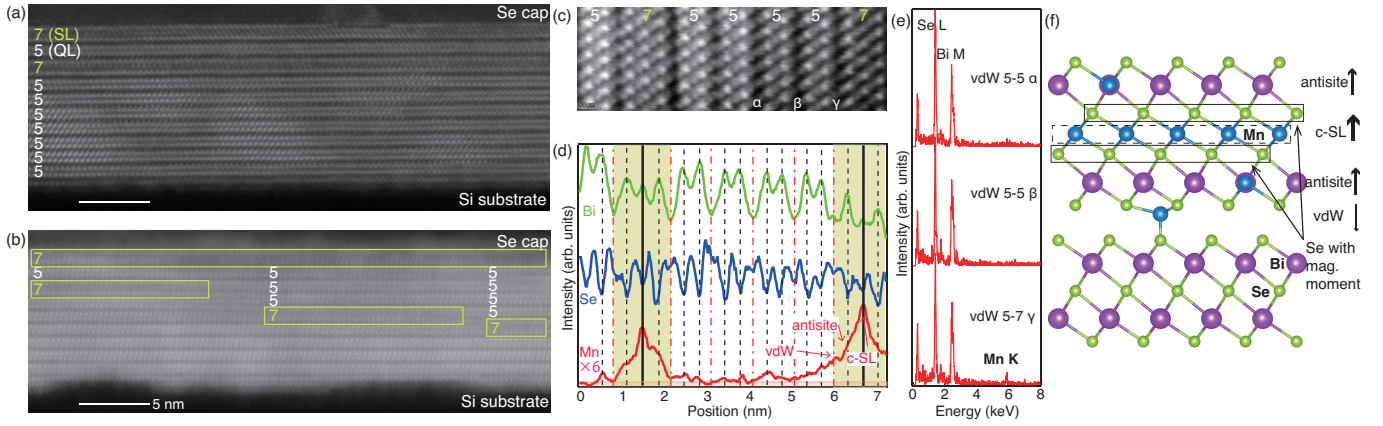


FIG. 1. (a, b) STEM image of the MBS / n QL BS / MBSBS sample for $n = 1$ (a) and 3 (b), respectively. (c) Close-up image of the $n = 4$ region seen on the right of panel (b). (d) EDS mapping of (c), showing the chemical composition of the heterostructure. Mn can not only be found in the central layer of the SL (c-SL), but is intermixed with Bi (antiseite Mn) as well as reside inside the vdW gap. The Mn spectrum has been enhanced by a factor of six. (e) Energy-dispersive X-ray spectra at the vdW gap of different positions in the sample indicated in (c). Whereas the Mn peak is absent at the vdW gap between 2 QLs, a clear Mn peak can be detected at the SL-QL vdW gap. (f) Schematic drawing of the Mn distribution inside the MBSBS heterostructure. The arrows show the mutual alignments of the local magnetic moments at the three different Mn sites, as deduced from the comparison of measured and calculated XAS and XMCD spectra. The Se layers with finite magnetic moment are also indicated.

of different structures that is observed is shown in Figs. S1 (b)-(e) of the Supplementary Material [60]. Thus our STEM measurements suggest that although the heterostructure samples are mostly the same as our original design of Fig. S1 (a), other structures can coexist and one needs to take this into account when performing macroscopic measurements. We also found that variation in n was larger for samples designed for larger n . This fact is particularly important to discuss the band structure of these samples as is scrutinized in Figs. S2 and S3.

Next, we concentrate on the actual atomic composition of the heterostructures. Figure 1(c) shows the high-resolution high-angle annular dark field STEM (HAADF-STEM) image taken from the [110] direction of the $n = 4$ region. Figure 1(d) shows the results of Energy-dispersive X-ray spectroscopy (EDS) measurements. To emphasize the distribution of Mn, the curve for Mn has been multiplied by a factor of six. As anticipated from the original design, Mn mainly lies at the center of the SL (c-SL). The position of Bi and Se seems to be also the same as the designed structure. However, a detailed inspection shows that the width of the Mn peak shown in Fig. 1(d) is broad and not only limited to the center of the SL but extends into the adjacent layers. Particularly, it seems that Mn can intermix in the Bi layers which we will call “antiseite Mn”. Furthermore, the Mn signal still seems to be larger than the background intensity even further away from the center of the SL, extending to the vdW gap between adjacent Se atoms. To verify this characteristic more vividly, Fig. 1(e) shows the EDS spectra at the vdW gap at three different positions of Fig. 1(c). While peaks that correspond to Se L and Bi M transitions can be identified in all the spectra shown, the Mn K peak is only detected at the SL-QL vdW gap. This clearly shows that Mn atoms can reside even in the vdW gap of the heterostructures of MBS and BS. Although magnetic atoms have been known to reside in the vdW gaps for doped

samples [64, 65], to the best of our knowledge, this is the first experimental observation in the intrinsic magnetic TIs. Figure 1(f) summarizes the present findings. Ideally, Mn should only reside at the center of the MBS SL, but experimentally it can intermix with Bi as well as reside in the vdW gap.

As discussed above, it is known that the misplaced Mn atoms alter the magnetic property of the intrinsic magnetic TI. Therefore, to clarify the magnetic interaction between the different Mn sites, we performed XMCD measurements. Figure 2(a) shows the X-ray absorption spectroscopy (XAS) spectra taken at 6 K with a magnetic field of 5 T applied perpendicular to the sample at the Mn L edge for the MBS / 7 QL BS / MBSBS sample. μ_+ and μ_- correspond to the spectrum obtained with left and right-handed circularly polarized photons, respectively. The corresponding XMCD spectrum is also shown and a clear signal is detected both at the L_3 and L_2 edges. The XMCD intensity has been deduced by normalizing $\mu_+ - \mu_-$ with the magnitude of the peak intensity at the L_3 edge [the difference of the values of the averaged XAS spectrum at 635 eV (background), and at 640 eV (peak position)].

We now compare the averaged XAS and XMCD data with theory to verify the magnetism of Mn at different sites. As shown in Fig. S4, the shape of the XMCD spectra did not change significantly for different heterostructure samples as well as for different measurement conditions. This is probably because the spot size in the XMCD measurements is ~ 200 μm and regions with different n coexist in all the samples as well as the fact that the concentration of the misplaced Mn is nearly the same since the same sample fabrication procedure is employed. Thus we performed the calculation of the XAS and XMCD spectra for a single septuple layer MBS and compared to the experimental data. Figures 2(b)-(d) show the XAS and XMCD spectra for the Mn in the central atomic plane of the SL (b), at the Bi site (c), and in the vdW gap

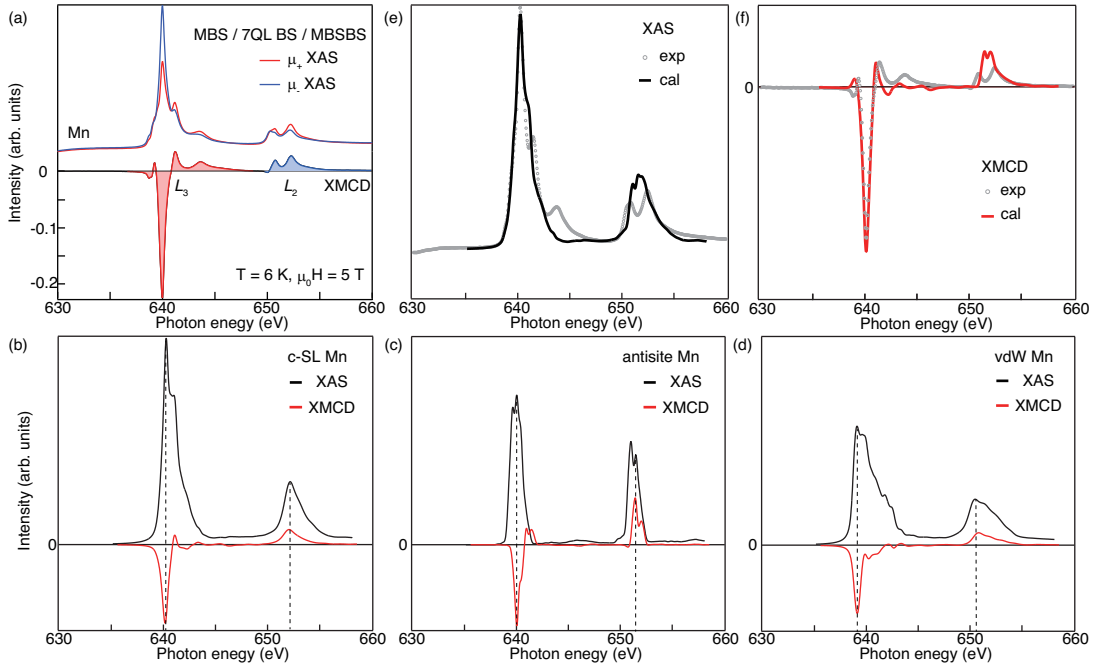


FIG. 2. (a) X-ray absorption spectra (XAS) measured at 6 K for a circularly polarized incident light when a magnetic field of 5 T was applied along the sample surface-normal direction for the MBS / 7 QL BS / MBSBS heterostructure at the Mn L edge. μ_+ and μ_- correspond to the spectrum obtained with left and right-handed circularly polarized photons, respectively. The corresponding XMCD spectra is also shown. (b-d) Calculated XAS and XMCD spectra for the Mn at the central layer in the SL (b), the Mn intermixed with Bi (antisite Mn) (c), and the Mn in the vdW gap (d), respectively. (e) Comparison of the experimental and calculated XAS spectra. The calculated spectrum is the convolution of the spectra shown in (b), (c), (d) with a ratio of 7 : 2 : 1. (f) Comparison of the experimental and calculated XMCD spectra. The calculated spectrum is the convolution of the spectra shown in (b), (c), (d) with a ratio of 7 : 2 : -1.

(d), respectively. The Mn valence in these sites is +2, +2, and +3, respectively. For the antisite Mn and Mn at the vdW gap, the Mn portion was set at 10 %. It can be easily noticed that the experimental data in Fig. 2(a) cannot be reproduced by considering c-SL Mn alone (Fig. 2(b)) and one needs to consider Mn at different sites. To be more specific, the former can only show a single peak for the L_2 edge, whereas in the experiment there are clearly two peaks. Quantitatively, we notice that the energy position of the largest XMCD signal is not the same for different Mn sites, as indicated by the dotted lines in Fig. 2(b)-(d).

We have tried to convolute the calculated spectra of the three different Mn sites and reproduce the experimental XAS and XMCD curves, as shown in Figs. 2(e) and (f). We could not obtain a perfect match, but the overall consistency was good when the ratio between the three Mn components of Figs. 2(b)-(d) was 6-7 : 3-2 : 1 for the XAS spectra (Fig. S5) [66]. The spectra shown in Fig. 2(e) is the case for a ratio of 7 : 2 : 1, whereas it is 7 : 2 : -1 in the XMCD spectrum in Fig. 2(f). The meaning of the plus (minus) sign is that the magnetic coupling is FM (AFM). Comparison of the experimental and convoluted theoretical XMCD spectra for various magnetic coupling scenarios is shown in Fig. S5. The important conclusion from this analysis is that the antisite Mn is coupled FM to the c-SL Mn whereas the vdW Mn is AFM coupled to the former two (Fig. 1(f)). This is in contrary to the case of MBT, where the c-SL Mn and antisite Mn were

shown to couple AFM and can diminish the DC gap in the band dispersion [14].

To verify if this conclusion can be reproduced by a different approach, we have calculated the Heisenberg exchange coupling constants directly using the magnetic force theorem for MBT and MBS/BS, as shown in Fig. 3. The exchange interactions of the c-SL Mn with antisite Mn atoms in MBT and MBSBS, as well as with the vdW Mn atoms in MBSBS, are shown. Note that the patterns of the $J_{0j}(r_{0j})$ dependence for the two systems are different because there are no Mn atoms in the vdW gap in the MBT case. It can be seen from the figure that in both systems the J_{01} parameters are positive, indicating FM coupling between the nearest neighbors inside the c-SL Mn layers. However, for the interactions between the c-SL and antisite Mn atoms the opposite signs of J_{0j} are revealed. While in MBT these parameters are negative (J_{02} and J_{03}), indicating the AFM coupling in agreement with experiment [13, 67], in MBSBS they are positive (J_{02} and J_{04}), meaning the FM coupling. Moreover, for MBSBS the AFM coupling between the c-SL Mn and that in the vdW gap is revealed, as both J_{03} and J_{05} are negative. Thus, the results of the magnetic force theorem calculations for the c-SL Mn coupling to the antisite and vdW Mn are in agreement with the conclusions drawn from the fitting of the experimental XMCD curves by the calculated ones.

To elucidate why the signs of the exchange integrals for the couplings with antisites in MBSBS are opposite to those

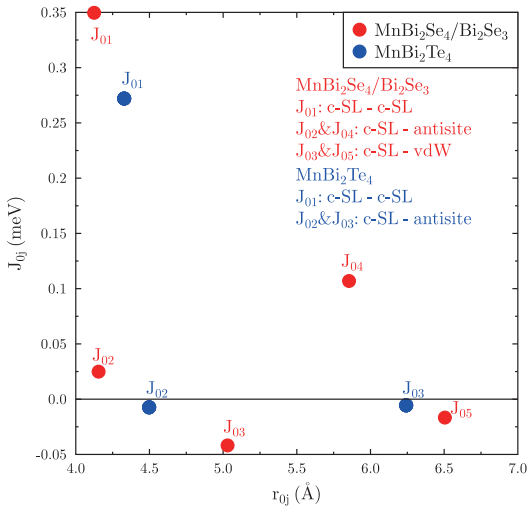


FIG. 3. Calculated Heisenberg exchange coupling constants J_{0j} for the Mn-Mn pair interactions as a function of the distance $r_{\text{Mn(c-SL)-Mn}(j)}$ for MBT (blue circles) and MBSBS (red circles). The interactions with the atoms from the neighboring SL blocks are not shown. As indicated in the legend, the c-SL - antisite interactions are described by J_{02} and J_{03} in MBT, while in MBSBS they correspond to J_{02} and J_{04} . This is because in MBSBS there Mn atoms in the vdW gap, their couplings to c-SL Mn being described by J_{03} and J_{05} .

of MBT, we have further analyzed the electronic densities of states. As it can be seen in Fig. 4, the hybridization of the antisite Mn $3d$ states with the Bi and Se states in MBSBS is stronger than that with Bi and Te states in MBT. The stronger hybridization can be explained by shorter interatomic distances in MBSBS that, as a result, enhances indirect double-exchange interaction between the local magnetic moments.

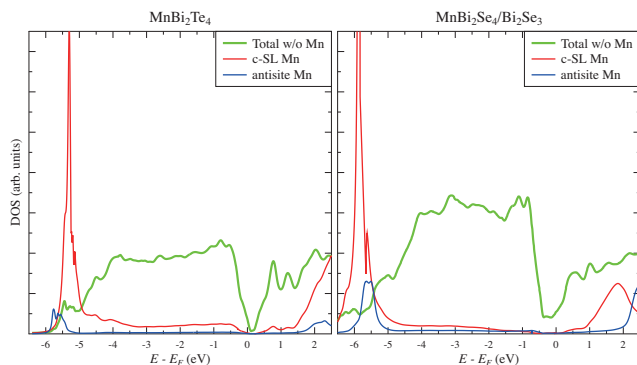


FIG. 4. Calculated density of states (DOS) of MBT (left) and MBSBS (right). The green curves show the sums of the projected DOSs of all Bi and Se atoms, while the red and blue ones – the projected DOSs of c-SL Mn and antisite Mn, respectively. The calculations are made taking spin-orbit coupling into account.

Now we will try to unveil the role of the nonmagnetic elements in these systems. Since measuring small XMCD signals for nonmagnetic elements is known to be extremely difficult [37, 68, 69], we have performed careful XAS/XMCD mea-

surements at 6 K with a magnetic field of 10 T applied perpendicular to the sample at the Se L edge for the MBS / 7 QL BS / MBSBS sample, as shown in Fig. 5(a). The XMCD intensity has been deduced by normalizing $\mu_+ - \mu_-$ with the magnitude of the peak intensity at the L_3 edge [the difference of the value of the averaged XAS spectrum at 1431 eV (background) and 1447 eV (peak)]. One can notice that finite XMCD signals arise at the L_3 and L_2 absorption edges. It seems that the peak structure is complex and the signal for both edges contain a pair of positive and negative peaks. To show that this signal is not an artifact, we show the Se XMCD spectra for different samples as well as the spectrum measured at different conditions in a separate facility in Fig. 5(b). Qualitatively, we can say that the prominent pair peak structure for different samples are the same and are sure that this signal is a real signal of Se magnetization. Compared to the results of similar measurements performed at the same beamline in SPring-8 (Ref. [68]) or ALBA (Ref. [69]) that report the absence of XMCD signals at the Se L edge, we are sure that the signals observed are finite and not an artifact. We emphasize that this kind of XMCD signal in nonmagnetic elements has been reported for Heusler alloys [70] or magnetic impurity-doped TIs [40–42]. However, this is the first example of a clear detection of the magnetic moment of a nonmagnetic element in intrinsic magnetic TIs, directly showing the magnetic interaction with the Mn layer. We also note that a very unclear XMCD signal was detected at the Bi N edge ($4d \rightarrow 6p$) as shown in Fig. S6 and the reason for this maybe that the peak signal of the XAS spectra itself is quite weak in Bi.

By carefully comparing the XAS and XMCD spectra, one notices that the peak at lower photon energy in the XMCD spectrum appears prior to the main absorption for both the L_3 and L_2 edges, as colored in green. These pre-edge peaks are opposite in sign with the main peaks colored in red and blue and moreover, their intensity is nearly the same order of magnitude as the main peaks. In addition, the sign of the XMCD signal is the opposite between the Mn and Se for the main peaks, thus suggesting that the Mn and Se are AFM coupled, consistent with what has been theoretically predicted in Ref. [6].

Figure 6(a) compares the experimental XAS data subtracted by the background with the calculation for the Se L edge [70]. The Se in this case corresponds to the atoms in the layer adjacent to central plane of the SL (i.e. Mn) and not those composing the vdW gap, as shown in Fig. 1(f). Although the calculation shows fine features not observed in the experiment, we can say that the two are consistent concerning the largest peaks. Figure 6(b) shows the comparison between the experimental and calculated XMCD signals and again the consistency between the two is good, further reinforcing the fact that the experimentally observed signal at the Se L edge is not an artifact. However, the pre-edge signal is somewhat weaker for the calculated spectrum.

Since the main peak of the L edge should correspond to the $2p \rightarrow 4d$ transition, it is possible that the pre-edge peak which is at ~ 2 eV smaller photon energy with opposite sign, include the contribution from the $2p \rightarrow 4s$ transition, since the change of the angular momentum in the transition is the op-

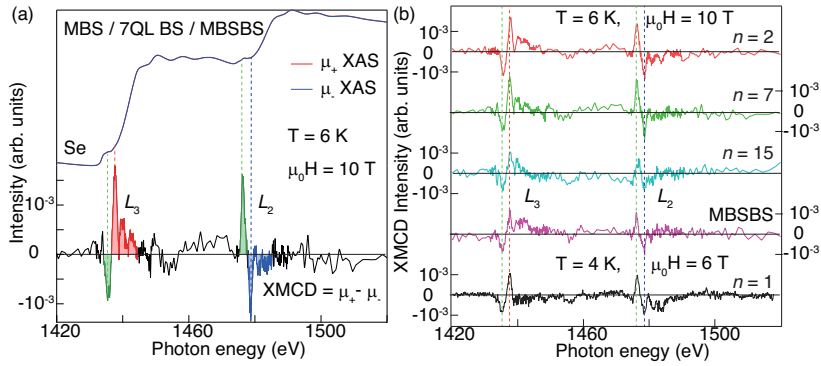


FIG. 5. (a) X-ray absorption spectra (XAS) measured at 6 K for a circularly polarized incident light when a magnetic field of 10 T was applied along the sample surface-normal direction for the MBS / 7 QL BS/ MBSBS heterostructure at the Se L edge. The corresponding XMCD spectra is also shown, indicating the clear detection of the Se magnetization. The red and blue main peaks likely correspond to the $2p \rightarrow 4d$ transition and the green pre-edge peaks correspond to the $2p \rightarrow 4s$ transition. (b) Comparison of the XMCD spectra between the MBS / n QL BS / MBSBS heterostructures for $n = 1, 2, 7, 15$ and that of MBSBS.

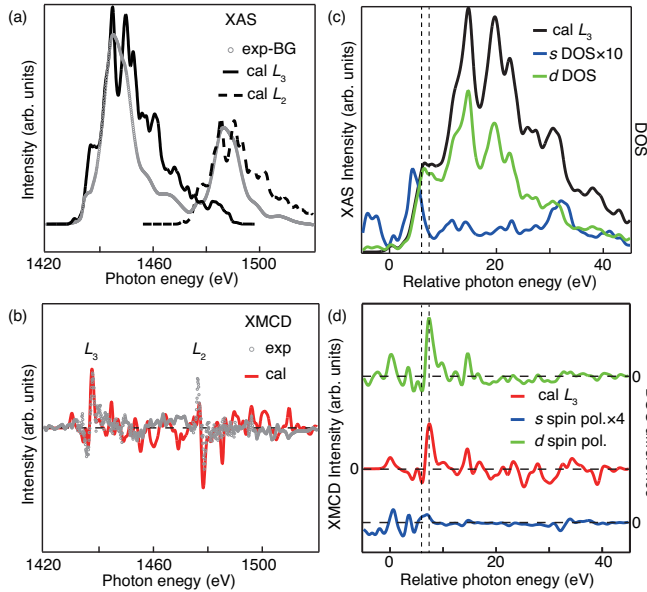


FIG. 6. (a,b) Comparison of the experimental XAS (a) and XMCD (b) spectra with the calculation at the Se L edge. (c) Comparison of the calculated XAS spectrum of the Se L_3 edge with the partial DOS of Se $4s$ and $4d$ orbitals. (d) Comparison of the calculated XMCD spectrum of the Se L_3 edge with the spin polarization (difference of the partial DOS of the majority and minority state) of Se $4s$ and $4d$ orbitals.

362 posite between $2p \rightarrow 4d$ (+1) and $2p \rightarrow 4s$ (-1). To test the
 363 above hypothesis, we first compare the calculated XAS spec-
 364 tra with the calculated spin-integrated unoccupied partial den-
 365 sity of state (PDOS) of the Se orbitals in the single MBS SL.
 366 Figure 6(c) shows the comparison between the XAS spectrum
 367 and the PDOS of Se $4s$ and $4d$ for the L_3 edge. The energy
 368 position has been shifted so that the spectral features of the $4d$
 369 DOS and XAS will coincide with each other. One can notice
 370 that the DOS of the s orbitals is much smaller than the d
 371 orbitals, and furthermore, the peak position of the s orbital is at

372 a smaller energy than the peaks for the d orbital. Figure 6(d)
 373 compares the calculated XMCD spectra with the DOS differ-
 374 ence between the majority and minority spin for the s and d
 375 orbitals. The DOS difference, which corresponds to the spin
 376 polarization of Se, is very small for both the s and d
 377 orbitals but finite values can be found at energies that are close to the
 378 peak positions in the XMCD spectrum. We can definitely say
 379 that the main peak originates from the spin polarization of the
 380 $4d$ states. For the pre-edge peak, although it is difficult to say
 381 that the spin-polarization of the s orbitals is giving the main
 382 contribution, its contribution should be larger than the main
 383 peak considering the larger DOS shown in Fig. 6(c). Thus we
 384 conclude that the main feature of the XMCD spectra of Se
 385 can be basically understood by the PDOS of the Se orbitals
 386 and the slight discrepancy between the experimental and theo-
 387 retical XMCD spectra should originate from the difference
 388 in the actual contribution of the s orbitals.

389 IV. CONCLUSION

390 In summary, we performed STEM and XMCD measure-
 391 ments on MBS / n QL BS / MBSBS heterostructures and
 392 found that the Mn atoms are not placed only in the central
 393 SL of MBS, but intermix with Bi as well as reside in the
 394 vdW gap. By comparing the experimentally measured XMCD
 395 spectra with theory, we find that the c-SL Mn and the antisite
 396 Mn are coupled ferromagnetically, whereas the vdW Mn
 397 are most likely coupled antiferromagnetically with the former
 398 two, which is different from the case of MBT. We also found
 399 clear evidence of the magnetic interaction of the Mn and Se
 400 from the detection of XMCD signal at the Se L edge. These
 401 results suggest the importance of identifying the magnetism of
 402 each elements at different environments in the intrinsic mag-
 403 netic TIs.

ACKNOWLEDGEMENT

We thank P. Gargiani and M. Valvidares for their assistance in the XMCD experiments. T.H. acknowledges the support by Grants-In-Aid from Japan Society for the Promotion of Science (Nos. 18H03877 and 22H00293), the Murata Science Foundation (No. H30-084), the Asahi Glass Foundation, the Iketani Science and Technology Foundation (0321083-A), and Support for Tokyo Tech Advanced Researchers. M.M.O. acknowledges the support by MCIN/AEI/10.13039/501100011033/ (Grant PID2022-138210NB-I00) and "ERDF A way of making Europe", by Ayuda CEX2023-001286-S financiada por MICIU/AEI/10.13039/501100011033, as well as MCIN with funding from European Union NextGenerationEU (PRTR-C17.I1) promoted by the Government of Aragon. S.V.E. acknowledge support from the Government

research assignment for ISPMS SB RAS, project FWRW-2022-0001. E.V.C. acknowledges Saint-Petersburg State University for a research project 95442847.

The ARPES measurements were performed under the UVSOR proposal Nos. 21-681, 21-867, 22IMS6661, and 22IMS6856. The XMCD measurements were performed at JAEA beamline BL-23SU in Spring-8 (Proposal Nos. 2020A3843, 2021A3843, and 2021B3843) and BL-29 BOREAS in ALBA (Proposal No. 2023027296). The work at Spring-8 was performed under the Shared Use Program of JAEA Facilities (Proposal Nos. 2020A-E16, 2021A-E19, and 2021B-E16) with the approval of Nanotechnology Platform project supported by the Ministry of Education, Culture, Sports, Science and Technology (Proposal Nos. JPMXP09A20AE0016, JPMXP09A21AE0017, and JPMXP09A21AE0036).

- [1] Y. Tokura, K. Yasuda, and A. Tsukazaki, *Nat. Rev. Phys.* **1**, 126 (2019).
- [2] F. D. M. Haldane, *Phys. Rev. Lett.* **61**, 2015 (1988).
- [3] C. Z. Chang, J. Zhang, X. Feng, J. Shen, Z. Zhang, M. Guo, K. Li, Y. Ou, P. Wei, L. L. Wang, Z. Q. Ji, Y. Feng, S. Ji, X. Chen, J. Jia, X. Dai, Z. Fang, S. C. Zhang, K. He, Y. Wang, L. Lu, X. C. Ma, and Q. K. Xue, *Science* **340**, 167 (2013).
- [4] X.-L. Qi, T. L. Hughes, and S.-C. Zhang, *Phys. Rev. B* **78**, 195424 (2008).
- [5] M. Mogi, Y. Okamura, M. Kawamura, R. Yoshimi, K. Yasuda, A. Tsukazaki, K. S. Takahashi, T. Morimoto, N. Nagaosa, M. Kawasaki, Y. Takahashi, and Y. Tokura, *Nat. Phys.* **18**, 390 (2022).
- [6] T. Hirahara, S. V. Eremeev, T. Shirasawa, Y. Okuyama, T. Kubo, R. Nakanishi, R. Akiyama, A. Takayama, T. Hajiri, S. Ideta, M. Matsunami, K. Sumida, K. Miyamoto, Y. Takagi, K. Tanaka, T. Okuda, T. Yokoyama, S. Kimura, S. Hasegawa, and E. V. Chulkov, *Nano Lett.* **17**, 3493 (2017).
- [7] T. Hirahara, M. M. Otrokov, T. T. Sasaki, K. Sumida, Y. Tomohiro, S. Kusaka, Y. Okuyama, S. Ichinokura, M. Kobayashi, Y. Takeda, K. Amemiya, T. Shirasawa, S. Ideta, K. Miyamoto, K. Tanaka, S. Kuroda, T. Okuda, K. Hono, S. V. Eremeev, and E. V. Chulkov, *Nat. Comm.* **11**, 4821 (2020).
- [8] M. M. Otrokov, I. I. Klimovskikh, H. Bentmann, D. Estyunin, A. Zeugner, Z. S. Aliev, S. Gaß, A. U. B. Wolter, A. V. Koroleva, A. M. Shikin, M. Blanco-Rey, M. Hoffmann, I. P. Rusinov, A. Yu. Vyazovskaya, S. V. Eremeev, Yu. M. Koroteev, V. M. Kuznetsov, F. Freyse, J. Sánchez-Barriga, I. R. Amiraslanov, M. B. Babanly, N. T. Mamedov, N. A. Abdullayev, V. N. Zverev, A. Alfonsov, V. Kataev, B. Büchner, E. F. Schwier, S. Kumar, A. Kimura, L. Petaccia, G. D. Santo, R. C. Vidal, S. Schatz, K. Kißner, M. Ünzelmann, C. H. Min, S. Moser, T. R. F. Peixoto, F. Reinert, A. Ernst, P. M. Echenique, A. Isaeva, and E. V. Chulkov, *Nature* **576**, 416 (2019).
- [9] I. I. Klimovskikh, M. M. Otrokov, D. Estyunin, S. V. Eremeev, S. O. Filnov, A. Koroleva, E. Shevchenko, V. Voroshnin, A. G. Rybkin, I. P. Rusinov, M. Blanco-Rey, M. Hoffmann, Z. S. Aliev, M. B. Babanly, I. R. Amiraslanov, N. A. Abdullayev, V. N. Zverev, A. Kimura, O. E. Tereshchenko, K. A. Kokh, L. Petaccia, G. D. Santo, A. Ernst, P. M. Echenique, N. T. Mamedov, A. M. Shikin, and E. V. Chulkov, *npj Quantum Mat.* **5**, 54 (2020).
- [10] Y. Liu, L.-L. Wang, Q. Zheng, Z. Huang, X. Wang, M. Chi, Y. Wu, B.C. Chakoumakos, M.A. McGuire, B.C. Sales, W. Wu, J. Yan, *Phys Rev X* **11**, 021033 (2021).
- [11] Y. Lai, L. Ke, J. Yan, R. D. McDonald, and R. J. McQueeney, *Phys Rev B* **103**, 184429 (2021).
- [12] S. X. M. Riberolles, Q. Zhang, Elijah Gordon, N. P. Butch, Liqin Ke, J.-Q. Yan, and R. J. McQueeney, *Phys. Rev. B* **104**, 064401 (2021).
- [13] M. Sahoo, I. Onuorah, L. Folkers, E. Chulkov, M. Otrokov, Z. Aliev, I. Amiraslanov, B. Büchner, L. Corredor, Ch. Wang, Z. Salman, A. Isaeva, R. De Renzi, and G. Allodi, *arXiv:2402.06340*.
- [14] M. Garnica, M. M. Otrokov, P. C. Aguilar, I. I. Klimovskikh, D. Estyunin, Z. S. Aliev, I. R. Amiraslanov, N. A. Abdullayev, V. N. Zverev, M. B. Babanly, N. T. Mamedov, A. M. Shikin, A. Arnau, A. L. V. de Parga, E. V. Chulkov, and R. Miranda, *npj Quan. Mat.* **7**, 7 (2022).
- [15] E. D. L. Rienks, S. Wimmer, J. Sánchez-Barriga, O. Caha, P. S. Mandal, J. Růžička, A. Ney, H. Steiner, V. V. Volobuev, H. Groiss, M. Albu, G. Kothleitner, J. Michalička, S. A. Khan, J. Minár, H. Ebert, G. Bauer, F. Freyse, A. Varykhalov, O. Rader, and G. Springholz, *Nature* **576**, 423 (2019).
- [16] Y. Gong, J. Guo, J. Li, K. Zhu, M. Liao, X. Liu, Q. Zhang, L. Gu, L. Tang, X. Feng, D. Zhang, W. Li, C. Song, L. Wang, P. Yu, X. Chen, Y. Wang, H. Yao, W. Duan, Y. Xu, S.-C. Zhang, X. Ma, Q.-K. Xue, and K. He, *Chin. Phys. Lett.* **36**, 076801 (2019).
- [17] J. Wu, F. Liu, M. Sasase, K. Ienaga, Y. Obata, R. Yukawa, K. Horiba, H. Kumigashira, S. Okuma, T. Inoshita, H. Hosono, *Sci. Adv.* **5**, eaax9989 (2019).
- [18] Y.-J. Hao, P. Liu, Y. Feng, X.-M. Ma, E. F. Schwier, M. Arita, S. Kumar, C. Hu, R. Lu, M. Zeng, Y. Wang, Z. Hao, H.-Y. Sun, K. Zhang, J. Mei, N. Ni, L. Wu, K. Shimada, C. Chen, Q. Liu, and C. Liu, *Phys. Rev. X* **9**, 041038 (2019).
- [19] H. Li, S.-Y. Gao, S.-F. Duan, Y.-F. Xu, K.-J. Zhu, S.-J. Tian, J.-C. Gao, W.-H. Fan, Z.-C. Rao, J.-R. Huang, J.-J. Li, D.-Y. Yan, Z.-T. Liu, W.-L. Liu, Y.-B. Huang, Y.-L. Li, Y. Liu, G.-B. Zhang, P. Zhang, T. Kondo, S. Shin, H.-C. Lei, Y.-G. Shi, W.-T. Zhang, H.-M. Weng, T. Qian, and H. Ding, *Phys. Rev. X* **9**, 041039 (2019).
- [20] Y. J. Chen, L. X. Xu, J. H. Li, Y. W. Li, H. Y. Wang, C. F. Zhang, H. Li, Y. Wu, A. J. Liang, C. Chen, S. W. Jung, C. Cacho, Y.

- H. Mao, S. Liu, M. X. Wang, Y. F. Guo, Y. Xu, Z. K. Liu, L. X. Yang, and Y. L. Chen, *Phys. Rev. X* **9**, 041040 (2019).
- [21] B. Chen, F. Fei, D. Zhang, B. Zhang, W. Liu, S. Zhang, P. Wang, B. Wei, Y. Zhang, Z. Zuo, J. Guo, Q. Liu, Z. Wang, X. Wu, J. Zong, X. Xie, W. Chen, Z. Sun, S. Wang, Y. Zhang, M. Zhang, X. Wang, F. Song, H. Zhang, D. Shen, and B. Wang, *Nat. Comm.* **10**, 4469 (2019).
- [22] P. Swatek, Y. Wu, L.-L. Wang, K. Lee, B. Schrunk, J. Yan, and A. Kaminski, *Phys. Rev. B* **101**, 161109(R) (2020).
- [23] S. H. Lee, Y. Zhu, Y. Wang, L. Miao, T. Pillsbury, H. Yi, S. Kempinger, J. Hu, C. A. Heikes, P. Quarterman, W. Ratcliff, J. A. Borchers, H. Zhang, X. Ke, D. Graf, N. Alem, C.-Z. CHANG, N. Samarth, and Z. Mao, *Phys. Rev. Research* **1**, 012011(R) (2019).
- [24] A. M. Shikin, T. P. Makarova, A. V. Eryzhenkov, D. Y. Usachov, D. A. Estyunin, D. A. Glazkova, I. I. Klimovskikh, A. G. Rybkin, and A. V. Tarasov, *Physica B* **645**, 414443 (2023).
- [25] A. M. Shikin, D. A. Estyunin, N. L. Zaitsev, D. Glazkova, I. I. Klimovskikh, S. O. Filnov, A. G. Rybkin, E. F. Schwier, S. Kumar, A. Kimura, N. Mamedov, Z. Aliev, M. B. Babanly, K. Kokh, O. E. Tereshchenko, M. M. Otrokov, E. V. Chulkov, K. A. Zvezdin, and A. K. Zvezdin, *Phys. Rev. B* **104**, 115168 (2021).
- [26] F. Lüpke, M. Kolmer, J. Yan, H. Chang, P. Vilmercati, H.H. Weitering, W. Ko, A.-P. Li, *Communications Materials* **4**, 82 (2023).
- [27] M. Liu, C. Lei, H. Kim, Y. Li, L. Frammolino, J. Yan, A.H. Macdonald, C.K. Shih, *Proc. Natl. Acad. Sci. U.S.A.* **119**, e2207681119 (2022).
- [28] Q. Li, I. Di Bernardo, J. Maniatis, D. McEwen, A. Dominguez-Celorrrio, M.T.H. Bhuiyan, M. Zhao, A. Tadich, L. Watson, B. Lowe, and others, *Advanced Materials* **36**, 2312004 (2024).
- [29] S. Wimmer, J. Sanchez-Barriga, P. Kuppers, A. Ney, E. Schierle, F. Freyse, O. Caha, J. Michalicka, M. Liebmann, D. Primetzhofer, M. Hoffmann, A. Ernst, M. M. Otrokov, G. Bihlmayer, E. Weschke, B. Lake, E. V. Chulkov, M. Morgenstern, G. Bauer, G. Springholz and O. Rader, *Adv. Mater.* **33**, 2102935 (2021).
- [30] P. Küppers, J. Zenner, S. Wimmer, G. Springholz, O. Rader, M. Liebmann, M. Morgenstern, *arXiv preprint arXiv:2202.11540* (2022).
- [31] R.C. Walko, T. Zhu, A.J. Bishop, R.K. Kawakami, J.A. Gupta, *Physica E: Low-dimensional Systems and Nanostructures* **143**, 115391 (2022).
- [32] T. Zhu, A. J. Bishop, T. Zhou, M. Zhu, D. J. O' Hara, A. A. Baker, S. Cheng, R. C. Walko, J. J. Repicky, T. Liu, J. A. Gupta, C. M. Jozwiak, E. Rotenberg, J. Hwang, I. Zutic, and R. K. Kawakami, *Nano Lett.* **21**, 5083 (2021).
- [33] A. M. Shikin, D. A. Estyunin, I. I. Klimovskikh, S. O. Filnov, E. F. Schwier, S. Kumar, K. Miyamoto, T. Okuda, A. Kimura, K. Kuroda, K. Yaji, S. Shin, Y. Takeda, Y. Saitoh, Z. S. Aliev, N. T. Mamedov, I. R. Amiraslanov, M. B. Babanly, M. M. Otrokov, S. V. Eremeev, and E. V. Chulkov, *Sci. Rep.* **10**, 13226 (2020).
- [34] P. Kagerer, C. I. Fornari, S. Buchberger, T. Tschirner, L. Veyrat, M. Kamp, A. V. Tcakaev, V. Zabolotnyy, S. L. Morelhão, B. Geldiyev, S. Müller, A. Fedorov, E. Rienks, P. Gargiani, M. Valvidares, L. C. Folkers, A. Isaeva, B. Büchner, V. Hinkov, R. Claessen, H. Bentmann, and F. Reinert, *Phys. Rev. Res.* **5**, L022019 (2023).
- [35] P. Kagerer, C. I. Fornari, S. Buchberger, S. L. Morelhão, R. C. Vidal, A. Tcakaev, V. Zabolotnyy, E. Weschke, V. Hinkov, M. Kamp, B. Büchner, A. Isaeva, H. Bentmann, and F. Reinert, *J. Appl. Phys.* **128**, 135303 (2020).
- [36] R. C. Vidal, A. Zeugner, J. I. Facio, R. Ray, M. H. Haghghi, A. U. B. Wolter, L. T. C. Bohorquez, F. Cagliaris, S. Moser, T. Figgemeier, T. R. F. Peixoto, H. B. Vasili, M. Valvidares, S. Jung, C. Cacho, A. Alfonso, K. Mehlatat, V. Kataev, C. Hess, M. Richter, B. Büchner, J. van den Brink, M. Ruck, F. Reinert, H. Bentmann, and A. Isaeva, *Phys. Rev. X* **9**, 041065 (2019).
- [37] A. Tcakaev, B. Rubrecht, J. I. Facio, V. B. Zabolotnyy, L. T. Corredor, L. C. Folkers, E. Kochetkova, T. R. F. Peixoto, P. Kagerer, S. Heinze, H. Bentmann, R. J. Green, P. Gargiani, M. Valvidares, E. Weschke, M. W. Haverkort, F. Reinert, J. van den Brink, B. Büchner, A. U. B. Wolter, A. Isaeva, and V. Hinkov, *Adv. Sci.* **10**, 2203239 (2023).
- [38] S. Wimmer, J. Sánchez-Barriga, P. Küppers, A. Ney, E. Schierle, F. Freyse, O. Caha, J. Michalicka, M. Liebmann, D. Primetzhofer, M. Hoffman, A. Ernst, M. M. Otrokov, G. Bihlmayer, E. Weschke, B. Lake, E. V. Chulkov, M. Morgenstern, G. Bauer, G. Springholz, and O. Rader, *Adv. Mater.* **33**, e2102935 (2021).
- [39] A. Tcakaev, B. Rubrecht, J. I. Facio, V. B. Zabolotnyy, L. T. Corredor, L. C. Folkers, E. Kochetkova, T. R. F. Peixoto, P. Kagerer, S. Heinze, H. Bentmann, R. J. Green, P. Gargiani, M. Valvidares, E. Weschke, M. W. Haverkort, F. Reinert, J. van den Brink, B. Büchner, A. U. B. Wolter, A. Isaeva, and V. Hinkov, *Adv. Sci.* **10**, 2203239 (2023).
- [40] M. Ye, T. Xu, G. Li, S. Qiao, Y. Takeda, Y. Saitoh, S.-Y. Zhu, M. Nurmatam, K. Sumida, Y. Ishida, S. Shin, and A. Kimura, *Phys. Rev. B* **99**, 144413 (2019).
- [41] M. Ye, W. Li, S. Zhu, Y. Takeda, Y. Saitoh, J. Wang, H. Pan, M. Nurmatam, K. Sumida, F. Ji, Z. Liu, H. Yang, Z. Liu, D. Shen, A. Kimura, S. Qiao, and X. Xie, *Nat. Comm.* **6**, 8913 (2015).
- [42] M. F. Islam, C. M. Canali, A. Pertsova, A. Balatsky, S. K. Mahatha, C. Carbone, A. Barla, K. A. Kokh, O. E. Tereshchenko, E. Jiménez, N. B. Brookes, P. Gargiani, M. Valvidares, S. Schatz, T. R. F. Peixoto, H. Bentmann, F. Reinert, J. Jung, T. Bathon, K. Fauth, M. Bode, and P. Sessi, *Phys. Rev. B* **97**, 155429 (2018).
- [43] Y. Saitoh, Y. Fukuda, Y. Takeda, H. Yamagami, S. Takahashi, Y. Asano, T. Hara, K. Shirasawa, M. Takeuchi, T. Tanaka, and H. Kitamura, *J. Synchrotron Radiat.* **19**, 388 (2012).
- [44] A. Barla, J. Nicolás, D. Cocco, S. M. Valvidares, J. Herrero-Martín, P. Gargiani, J. Moldes, C. Ruget, E. Pellegrin and S. Ferrer, *J. Synchrotron Radiat.* **23**, 1507–1517 (2016).
- [45] P. E. Blöchl, *Phys. Rev. B* **50**, 17953 (1994).
- [46] G. Kresse and J. Furthmüller, *Phys. Rev. B* **54**, 11169 (1996).
- [47] G. Kresse and D. Joubert, *Phys. Rev. B* **59**, 1758 (1999).
- [48] D. D. Koelling and B. N. Harmon, *Journal of Physics C: Solid State Physics* **10**, 3107 (1977).
- [49] J. P. Perdew, K. Burke and M. Ernzerhof, *Phys. Rev. Lett.* **77**, 3865 (1996).
- [50] S. Grimme, S. Ehrlich and L. Goerigk, *Journal of Computational Chemistry* **32**, 1456 (2011).
- [51] V. I. Anisimov, J. Zaanen and O. K. Andersen, *Phys. Rev. B* **44**, 943 (1991).
- [52] S. L. Dudarev, G. A. Botton, S. Y. Savrasov, C. J. Humphreys and A. P. Sutton, *Phys. Rev. B* **57**, 1505 (1998).
- [53] A. I. Liechtenstein, M. I. Katsnelson, V. P. Antropov, V. A. Gubanov, *Jour. Mag. Mag. Mat.* **67**, 65 (1987).
- [54] M. Hoffmann, A. Ernst, W. Hergert, V. N. Antonov, W. A. Adeagbo, R. M. Geilhufe, H. B. Hamed, *Physica Status Solidi (b)* **257**, 1900671 (2020).
- [55] M. Geilhufe, S. Achilles, M. A. Köbis, M. Arnold, I. Mertig, W. Hergert, A. Ernst, *Jour. Phys.: Cond. Mat.* **27**, 435202 (2015).
- [56] J. P. Perdew, A. Ruzsinszky, G. I. Csonka, O. A. Vydrov, G. E. Scuseria, L. A. Constantin, X. Zhou, and K. Burke, *Phys. Rev. Lett.* **100**, 136406 (2008).
- [57] P. Soven, *Phys. Rev.* **156**, 809 (1967).

- 647 [58] B. L. Gyorffy, Phys. Rev. B **5**, 2382 (1972).
648 [59] V. N. Antonov, B. N. Harmon, A. N. Yaresko, *Electronic struc-*
649 *ture and magneto-optical properties of solids*, Springer (2004).
650 [60] See the supplementary information at ... for details of the
651 sample atomic structure, the band dispersion measured by
652 ARPES in comparison to DFT calculations, and the details
653 of the XMCD analysis concerning the Mn *L* edge, and the
654 XMCD spectra for Bi. The Supplementary Material also con-
655 tains Refs. [61–63].
656 [61] S. Kimura, T. Ito, M. Sakai, E. Nakamura, N. Kondo, T.
657 Horigome, K. Hayashi, M. Hosaka, M. Katoh, T. Goto, T.
658 Ejima, K. Soda, Rev. Sci. Instrum. **81**, 053104 (2010).
659 [62] Y. Sakamoto, T. Hirahara, H. Miyazaki, S. Kimura, and S.
660 Hasegawa, Phys. Rev. B **81**, 165432 (2010).
661 [63] Y. Zhang, K. He, C.-Z. Chang, C.-L. Song, L.-L. Wang, X.
662 Chen, J.-F. Jia, Z. Fang, X. Dai, W.-Y. Shan, S.-Q. Shen, Q.
663 Niu, X.-L. Qi, S.-C. Zhang, X.-C. Ma, and Q.-K. Xue, Nat.
664 Phys. **6**, 584 (2010).
665 [64] M. M. Yee, Z.-H. Zhu, A. Soumyanarayanan, Y. He, C.-L.
666 Song, E. Pomjakushina, Z. Salman, A. Kanigel, K. Segawa, Y.
667 Ando, and J. E. Hoffman, Phys. Rev. B **91**, 161306 (R) (2015).
668 [65] J. Růžička, O. Caha, V. Holý, H. Steiner, V. Volobuev, A. Ney,
669 G. Bauer, T. Duchoň, K. Veltruská, I. Khalakhan, V. Matolín, E.
670 F. Schvier, H. Iwasawa, K. Shimada, and G. Springholz, New
671 Jour. Phys. **17**, 013028 (2015).
672 [66] The reason for the absence of a perfect match may be that the
673 XMCD calculations have been done in a single-particle pic-
674 ture while in reality, there should be many-body effects as well
675 as clustering of the Mn atoms in the experiment. Furthermore,
676 theory assumes broadening of the peak structure with finite life-
677 time, and this is not easy to predict perfectly. This is particularly
678 significant at ~ 644 eV in Fig. 2 (e); whereas only a shoulder
679 structure is seen for the calculation, it shows up as a clear peak
680 in the experimental XAS data.
681 Even when a more sophisticated calculation method is em-
682 ployed for a pure system, the theoretical and experimental
683 XMCD spectra cannot be perfectly matched, eg. Phys. Rev.
684 Lett. **132**, 176701 (2024).
685 [67] Y. Lai, L. Ke, J. Yan, R. D. McDonald, and R. J. McQueeney,
686 Phys. Rev. B **103**, 184429 (2021).
687 [68] K. Sumida, Y. Takeda, S. Kusaka, K. Kobayashi, and T. Hira-
688 hara, Phys. Rev. Mat. **6**, 014006 (2022).
689 [69] A. I. Figueroa, F. Bonell, M. G. Cuxart, M. Valvidares, P. Gar-
690 giani, G. van der Laan, A. Mugarza, and S. O. Valenzuela, Phys.
691 Rev. Lett. **125**, 226801 (2020).
692 [70] T. Yoshikawa, V. N. Antonov, T. Kono, M. Kakoki, K. Sum-
693 ida, K. Miyamoto, Y. Takeda, Y. Saitoh, K. Goto, Y. Sakuraba,
694 K. Hono, A. Ernst, and A. Kimura, Phys. Rev. B **102**, 064428
695 (2020).